Optimization and characterization of highly nonlinear fiber for broadband optical time lens applications.

Lillieholm, Mads; Guan, Pengyu; Galili, Michael; Møller-kristensen, M. S.; Grüner-Nielsen, L.; Oxenløwe, Leif Katsuo

Published in:
Optics Express

Link to article, DOI:
10.1364/OE.25.012566

Publication date:
2017

Document Version
Publisher's PDF, also known as Version of record

Research Article | Vol. 25, No. 11 | 29 May 2017 | OPTICS EXPRESS 12566
Optics EXPRESS

Optimization and characterization of highly nonlinear fiber for broadband optical time lens applications

M. Lillieholm,[1,*] P. Guan,[1] M. Galili,[1] M. S. Møller-Kristensen,[1] L. Grüner-Nielsen,[2] and L. K. Oxenløwe[1]

[1]DTU Fotonik, Technical University of Denmark, Bldg. 340, DK-2800 Kgs. Lyngby, Denmark
[2]Danish Optical Fiber Innovation, Åvendingen 22A, DK-2700 Brønshøj, Denmark
*madsl@fotonik.dtu.dk

Abstract: We demonstrate simple and intuitive methods, for dispersion optimization and characterization of highly nonlinear fiber (HNLF) for use in four-wave-mixing (FWM) based time lens applications. A composite dispersion-flattened HNLF is optimized for high bandwidth time lens processing, by segmentation to mitigate FWM impairments due to dispersion fluctuations. The fiber is used for FWM conversion of 32 WDM-channels with 50 GHz spacing in a time lens, with −4.6 dB total efficiency, and <1 dB per-channel efficiency difference. The novel characterization method is based on two tunable continuous-wave lasers. The method is experimentally verified to predict the spectral output profile of time lenses for broadband multicarrier input, with detailed numerical simulations for support.

OCIS codes: (190.4380) Nonlinear optics, four-wave mixing; (070.4340) Nonlinear optical signal processing; (260.2030) Dispersion; (060.2330) Fiber optics communications.

References and links

1. T. Jannson, "Real-time Fourier transformation in dispersive optical fibers," Opt. Lett. **8**(4), 232–234 (1983).
2. M. Nakazawa, T. Hirooka, F. Futami, and S. Watanabe, "Ideal distortion-free transmission using optical Fourier transformation and Fourier transform-limited optical pulses," IEEE Photonics Technol. Lett. **16**(4), 1059–1061 (2004).
3. B. H. Kolner, "Space-time duality and the theory of temporal imaging," IEEE J. Quantum Electron. **30**(8), 1951–1963 (1994).
4. L. F. Mollenauer and C. Xu, "Time-lens timing-jitter compensator in ultra-long haul DWDM dispersion managed soliton transmissions," in *Proceedings of Conference on Lasers and Electro-Optics*, OSA Technical Digest (Optical Society of America, 2002), pp. CPDB1.
5. M. A. Foster, R. Salem, D. F. Geraghty, A. C. Turner-Foster, M. Lipson, and A. L. Gaeta, "Silicon-chip-based ultrafast optical oscilloscope," Nature **456**(7218), 81–84 (2008).
6. H. C. H. Mulvad, E. Palushani, H. Hu, H. Ji, M. Lillieholm, M. Galili, A. T. Clausen, M. Pu, K. Yvind, J. M. Hvam, P. Jeppesen, and L. K. Oxenløwe, "Ultra-high-speed optical serial-to-parallel data conversion by time-domain optical Fourier transformation in a silicon nanowire," Opt. Express **19**(26), B825–B835 (2011).
7. P. Guan, S. Lefrancois, M. Lillieholm, H. C. H. Mulvad, K. M. Røge, H. Hu, J. Schröder, B. J. Eggleton, Z. Geng, A. J. Lowery, T. Morioka, and L. K. Oxenløwe, "All-optical OFDM system using a wavelength selective switch based transmitter and a spectral magnification based receiver," in *Proceedings of European Conference on Optical Communication*, ECOC (2014), pp. 1–3.
8. P. Guan, K. Meldgaard Roge, M. Lillieholm, M. Galili, H. Hu, T. Morioka, and L. Oxenloewe, "Time lens based optical Fourier transformation for all-optical signal processing of spectrally-efficient data," J. Lightwave Technol. **99**, 1 (2016).
9. P. Guan, F. Da Ros, M. Lillieholm, H. Hu, K. M. Røge, M. Galili, T. Morioka, and L. K. Oxenløwe, "16 channel WDM regeneration in a single phase-sensitive amplifier through optical fourier transformation," in *Proceedings of European Conference on Optical Communication,* ECOC (2016), paper Th.3.B.3.
10. K. Inoue, "Four-wave mixing in an optical fiber in the zero-dispersion wavelength region," J. Lightwave Technol. **10**(11), 1553–1561 (1992).
11. R. Salem, M. A. Foster, A. C. Turner, D. F. Geraghty, M. Lipson, and A. L. Gaeta, "Optical time lens based on four-wave mixing on a silicon chip," Opt. Lett. **33**(10), 1047–1049 (2008).
12. T. Torounidis, P. A. Andrekson, and B. E. Olsson, "Fiber-optical parametric amplifier with 70-dB gain," IEEE Photonics Technol. Lett. **18**(10), 1194–1196 (2006).
13. E. Palushani, L. K. Oxenløwe, M. Galili, H. C. H. Mulvad, A. T. Clausen, and P. Jeppesen, "Flat-top pulse generation by the optical fourier transform technique for ultrahigh speed signal processing," IEEE J. Quantum

#290350 https://doi.org/10.1364/OE.25.012566
Journal © 2017 Received 8 Mar 2017; revised 4 May 2017; accepted 10 May 2017; published 19 May 2017

Optics EXPRESS

Electron. **45**(11), 1317–1324 (2009).
14. H. Hu, D. Kong, E. Palushani, J. D. Andersen, A. Rasmussen, B. M. Sørensen, M. Galili, H. C. H. Mulvad, K. J. Larsen, S. Forchhammer, P. Jeppesen, and L. K. Oxenløwe, "1.28 Tbaud Nyquist signal transmission using time-domain optical fourier transformation based receiver," in *CLEO: Science and Innovations*, OSA Postdeadline Paper Digest (Optical Society of America, 2013), paper CTh5D.5.
15. M. E. Marhic, N. Kagi, T. K. Chiang, and L. G. Kazovsky, "Broadband fiber optical parametric amplifiers," Opt. Lett. **21**(8), 573–575 (1996).
16. T. Okuno, M. Hirano, T. Kato, M. Shigematsu, and M. Onishi, "Highly nonlinear and perfectly dispersion-flattened fibres for efficient optical signal processing applications," Electron. Lett. **39**(13), 972 (2003).
17. M. Lillieholm, M. Galili, L. Grüner-Nielsen, and L. K. Oxenløwe, "Detailed characterization of CW- and pulsed-pump four-wave mixing in highly nonlinear fibers," Opt. Lett. **41**(21), 4887–4890 (2016).
18. M. Karlsson, "Four-wave mixing in fibers with randomly varying zero-dispersion wavelength," J. Opt. Soc. Am. B **15**(8), 2269–2275 (1998).
19. R. S. Yuki Taniguchi, J. Hiroishi, and M. Takahashi, "Nonlinear optical fiber, nonlinear optical device, and optical signal processor," U.S. patent EP1988411A1 (2008).
20. B. P.-P. Kuo, J. M. Fini, L. Grüner-Nielsen, and S. Radic, "Dispersion-stabilized highly-nonlinear fiber for wideband parametric mixer synthesis," Opt. Express **20**(17), 18611–18619 (2012).
21. K. Inoue, "Arrangement of fiber pieces for a wide wavelength conversion range by fiber four-wave mixing," Opt. Lett. **19**(16), 1189–1191 (1994).
22. E. Myslivets, C. Lundström, J. M. Aparicio, S. Moro, A. O. J. Wiberg, C.-S. Bres, N. Alic, P. A. Andrekson, and S. Radic, "Spatial equalization of zero-dispersion wavelength profiles in nonlinear fibers," IEEE Photonics Technol. Lett. **21**(24), 1807–1809 (2009).
23. E. Myslivets, N. Alic, J. R. Windmiller, and S. Radic, "A new class of high-resolution measurements of arbitrary-dispersion fibers: Localization of four-photon mixing process," J. Lightwave Technol. **27**(3), 364–375 (2009).
24. M. Lillieholm, M. Galili, and L. K. Oxenløwe, "Dispersion-flattened composite highly nonlinear fibre optimised for broadband pulsed four-wave mixing," in *Proceedings of European Conference on Optical Communication*, (ECOC, 2016), pp. 330–332.
25. P. Guan, K. M. Røge, H. C. H. Mulvad, H. Hu, T. Morioka, and L. K. Oxenløwe, "Conversion of a DWDM signal to a single Nyquist channel based on a complete optical Fourier transformation," in *Proceedings of European Conference on Optical Communication* (ECOC, 2014), pp. 3–5.
26. H. C. H. Mulvad, H. Hu, M. Galili, H. Ji, E. Palushani, A. T. Clausen, L. K. Oxenløwe, and P. Jeppesen, "DWDM-to-OTDM conversion by time-domain optical Fourier transformation," in *Proceedings of European Conference on Optical Communication*, (ECOC, 2011), pp. 1–3.
27. O. V. Sinkin, R. Holzlohner, J. Zweck, and C. R. Menyuk, "Optimization of the split-step fourier method in modeling optical-fiber communications systems," J. Lightwave Technol. **21**(1), 61–68 (2003).
28. J. Hansryd, P. A. Andrekson, M. Westlund, J. Li, and P. O. Hedekvist, "Fiber-based optical parametric amplifiers and their applications," IEEE J. Sel. Top. Quantum Electron. **8**(3), 506–520 (2002).
29. L. S. Rishøj and K. Rottwitt, "Influence of variations of the GVD on wavelength conversion at second gain region of a parametric process," in *Advanced Photonics & Renewable Energy*, OSA Technical Digest (Optical Society of America, 2010), paper NTuC11.
30. L. Cohen, W. Mammel, and S. Lumish, "Dispersion and bandwidth spectra in single-mode fibers," IEEE J. Quantum Electron. **18**(1), 49–53 (1982).
31. S. K. Korotky, P. B. Hansen, L. Eskildsen, and J. J. Veselka, "Efficient phase modulation scheme for suppressing stimulated Brillouin scattering," in *Proceedings of. Integrated Optics and Optical Fiber Communications* (IOOC, 1995), pp. 108–111.

1. Introduction

The versatility of the optical Fourier transformation (OFT) [1,2], which can be obtained at the focal point of a time lens [3], has been shown by the many demonstrations of ultrafast advanced optical signal processing (OSP) [4–9]. Time lens theory originates with the space-time duality [3], which formulates the equivalence between thin lens refraction and quadratic phase modulation. The time lens is often implemented by four-wave mixing (FWM) [10], which enables extremely large phase shifts [11]. The FWM medium is e.g. highly nonlinear fiber (HNLF), which benefits from convenient system integration and the potential for high efficiency [12]. The pump typically consists of flat-top, linearly chirped pulses [13], with bandwidths up to 1.6 THz reported [14], and quasi continuous-wave (CW) characteristics in the time domain. The temporal time lens resolution improves with the pump bandwidth. However, the FWM bandwidth depends on a uniform phase mismatch for all significant chirped pump frequency content, which is reliant on a low third-order dispersion (TOD), β_3. Hence, it is challenging to simultaneously achieve large conversion bandwidth and efficiency

Optics EXPRESS

in a FWM-based time lens using a broadband pump. In principle, the FWM efficiency with a CW pump depends only on the even dispersion orders [15]. However, pulsed pumps are affected by the TOD, which e.g. exacerbates the effects of walkoff, and introduces a time dependent efficiency for chirped pulses. Hence, it is desirable to use HNLF with low TOD for time lens applications. However, HNLF engineered for low TOD, such as dispersion-flattened HNLF (DF-HNLF) [16], tends to exhibit very large longitudinal zero dispersion wavelength (ZDW) fluctuations [17], which limits the FWM bandwidth and efficiency [18]. Although some fiber designs have succeeded in enabling the fabrication of HNLF with very stable dispersion [19,20], the TOD tends to be significantly larger than for standard HNLF. Instead, techniques to manage dispersion fluctuations in HNLF have been demonstrated, including a destructive method where the phase mismatch is reduced by rearranging fiber segments with different local dispersion [21], and a nondestructive modification of the local dispersion by applying variable, local tensile stress [22]. The former technique is simple and allows for combination of different fibers types, although it relies on low-loss splicing and a certain distribution of the local dispersion to optimize the benefit. The latter technique can in principle improve the dispersion stability of arbitrary HNLF, and lower the stimulated Brillouin scattering (SBS) threshold at the same time. However, the technique requires relatively complex high-resolution, nondestructive dispersion mapping [23], and the strain may increase the polarization-mode dispersion [20]. Furthermore, standard FWM characterization methods do not allow for the accurate determination of the chirped pump bandwidth and efficiency in HNLF. As such, there is a need for a characterization method, which enables accurate FWM optimization in HNLF for time lens applications.

In this paper, we present both a simple method for the characterization of HNLF for time lens applications, and the demonstration of a composite DF-HNLF with optimized dispersion for efficient, broadband conversion in a time lens experiment. The characterization method is based on efficiency measurements from the mixing of two tunable CW laser sources, and employs a standard CW characterization setup. The proposed method is investigated using detailed numerical simulations, and experimentally verified to provide accurate characterizations for fibers used in two time lens experiments. The first experiment is the present demonstration of a composite DF-HNLF [24], for which uniform conversion of 32 wavelength-division multiplexing (WDM) channels with 50 GHz spacing is achieved using a 600-GHz bandwidth, chirped pump. A total input conversion efficiency of –4.6 dB is measured, and <1 dB channel conversion efficiency difference is indicated. The second time lens experiment is the previously reported conversion of 16 WDM channels in a standard HNLF as part of a "complete OFT" system [25], including new results for 8 channels.

2. Principle and study of CW characterization for chirped pump FWM in HNLF

The CW characterization method for HNLF for chirped-pump FWM, is investigated using detailed numerical simulations. In particular, the method will be used to predict the operating bandwidth and per-channel conversion efficiency of WDM to optical time-division multiplexing (WDM-OTDM) conversion by OFT [26]. An OFT system employing a time lens based on chirped-pump FWM, is illustrated spectrographically in Fig. 1. Here input WDM channels at frequencies ω_{si} are converted to idlers at ω_{ii}, using a linearly chirped pump at ω_p with bandwidth $\Delta\omega_p$. The pump with chirp rate $K/2$ imparts a quadratic phase modulation with chirp rate K on the idler via FWM, per $E_i \propto E_p^2 E_s^*$, which relates the optical idler field to the pump and signal fields. Chirped idler pulses at different wavelengths are then focused onto different time slots, by subsequent propagation in a medium with accumulated dispersion $D = \beta_2 L$ (not to be confused with the group velocity dispersion with respect to wavelength). Here β_2 is the second order group velocity dispersion and L the length of the medium. If the OFT condition, $K = 1/D$, is met, the interval between pulses at the OFT output, Δt, is related to the input WDM channel spacing, $\Delta\omega$, by $\Delta t = D\Delta\omega$. Due to the temporal spread of the pump frequencies, the local FWM interaction between the pump and

Optics EXPRESS

low-rate WDM subcarriers occurs only with a subset of the pump frequencies. Hence, the time lens efficiency can be emulated by a virtual decomposition of the chirped pump FWM process, into a set of constituent processes, driven by the mixing of a tunable CW pump- and signal-laser. To emulate the WDM-OTDM conversion efficiency, the pump and signal are positioned as indicated (circles) in Fig. 1. Here the CW signal is placed at each of the central WDM channel frequencies in turn, and the CW pump swept over the part of the pump bandwidth overlapping temporally with the signal, $\delta\omega_p$. It is indicated how the CW measurements can be combined to predict the shape of the idler spectrum, and we will show that the individual WDM channel conversion efficiencies can be estimated as well. Thus, the method offers low-complexity characterization of a complex system, and some features which are otherwise hidden can be exposed by the decomposition.

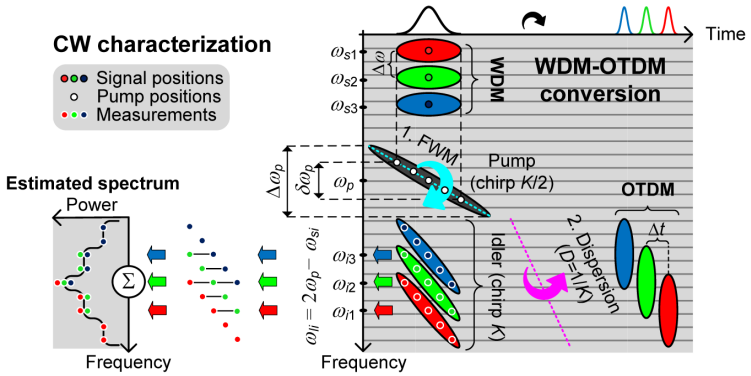

Fig. 1. Principle of WDM-OTDM conversion based on FWM, and indicated CW positions and measurement points for the characterization method (circles). Also shown is how the measurements are combined to estimate the idler.

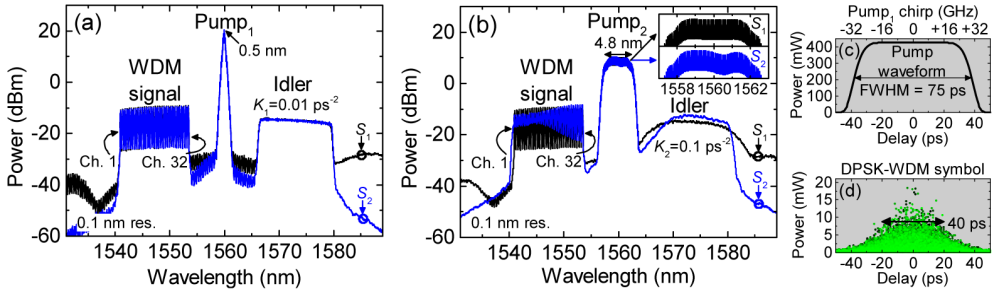

Fig. 2. (a) Simulated FWM spectra for conversion of the WDM signal with a 0.5-nm chirped pump. (b) FWM spectra for a 4.8-nm chirped pump, with insets showing pump zoom-ins. (c) Optical pump$_2$ waveform, (d) and WDM symbols.

For subsequent comparison with the CW characterization method, two cases of FWM between a 32-channel WDM signal and chirped pump pulses at different chirp rates, are simulated in two different HNLFs. The fibers are lossless and identical except for the dispersion slope values S_1 = 0.005 ps/(nm^2·km) (typical DF-HNLF value) and S_2 = 0.07 ps/(nm^2·km) (typical for HNLF engineered for low dispersion fluctuations). The remaining parameters are length L = 500 m, nonlinear coefficient γ = 10.8 (W·km)$^{-1}$, ZDW λ_0 = 1560 nm and fourth order dispersion $\beta_4 = 2.6 \times 10^{-4}$ ps^4/km. The fiber propagation is simulated on 256 WDM symbols and pump pulses with 10 GHz repetition rate, using a split-step Fourier method (SSFM) to solve the scalar nonlinear Schrödinger equation. The temporal resolution is <1 ps, and the adaptive step size is based on the local error [27]. The pump pulse shape is in both cases 10th order super-Gaussian with Δt_p = 75 ps full-width at half maximum (FWHM)

Optics EXPRESS

and P_p = 25 dBm average power, centered at wavelength $\lambda_p = \lambda_0$. The WDM signal is centered at λ_s = 1547 nm with 50 GHz channel spacing. The channels are independently return-to-zero (RZ) differential binary phase-shift keying (DPSK) modulated at 10 Gbit/s with random uniformly distributed bits, and random carrier phase. The data symbols are Gaussian with Δt_s = 40 ps FWHM and −15 dBm per-channel average power, and synchronized with the pump pulses at the HNLF input. The FWM spectra for Pump_1 with linear chirp $K_1/2 = 0.005$ ps^{-2} are shown for both fibers in Fig. 2(a). Here the chirp rate is defined as the ratio $\Delta\omega_p/\Delta t_p$. The 1-dB bandwidth of Pump_1 is $\Delta\lambda_{p,1}$ = 0.5 nm, and the observed idler spectra are almost identical for both fibers with only modest spectral broadening per channel. The spectra corresponding to Pump_2 (chirp rate $K_2/2 = 0.05$ ps^{-2}) are shown in Fig. 2(b), where the FWM results can be observed to differ significantly depending on the dispersion slope. The pump waveform with the Pump_1 chirp on the top horizontal axis (× 10 for Pump_2 chirp) is shown in Fig. 2(c). The superimposed WDM symbols are shown in Fig. 2(d). The 1-dB bandwidth of Pump_2 is $\Delta\lambda_{p,2}$ = 4.8 nm, i.e. 10 times larger than Pump_1. For Pump_2, the idlers experience large spectral broadening, with a high degree of asymmetry observed for S_2. The primary reason for the asymmetry is the pump-signal phase mismatch dependence on the local pump wavelength, due to the dispersion slope. The efficiency is locally high at a pump wavelength of ~1560.6 nm, as indicated by the small spectral depression due to pump depletion (see Fig. 2(b), S_2 inset). The efficiency dependence on the local pump wavelength carries into the time domain for a chirped pump, and hence the generated idler is distorted, with increasingly pronounced effect for channels at larger pump-signal detuning ($\lambda_s - \lambda_p$). Neglecting fourth order dispersion and higher, the phase mismatch due to dispersion expanded around λ_0, $\Delta\beta$, can be approximated by [28],

$$\Delta\beta = -\frac{2\pi c}{\lambda_0^2} S\left(\lambda_p - \lambda_0\right)\left(\lambda_s - \lambda_p\right)^2, \tag{1}$$

where c is the speed of light in vacuum. From Eq. (1), a simple expression can be derived for the phase mismatch difference at opposite ends of the pump spectrum, $\delta\beta_p$. I.e. for a chirped pump with bandwidth $\Delta\lambda_p << |\lambda_p - \lambda_s|$ near λ_0, we can obtain approximately,

$$\delta\beta_p \approx 2\pi c |S| \Delta\lambda_p \left(1 - \frac{\lambda_s}{\lambda_p}\right)^2. \tag{2}$$

Equation (2) shows that $\delta\beta_p$ scales with the dispersion variation over the pump bandwidth, $|S|\Delta\lambda_p$. At λ_0, $\beta_3 \propto S$, hence S represents the TOD for phase matching purposes. The FWM gain coefficient $g = (-\Delta\beta(\Delta\beta/4 + \gamma P_p))^{1/2}$ is real for $-4\gamma P_p \le \Delta\beta \le 0$, and purely imaginary otherwise. For imaginary g, the conversion efficiency $\eta_c = (\gamma P_p/g)^2 \sinh^2(gL)$ can be expressed as $(\gamma P_p)^2(\sin(\text{Im}(g)L)/\text{Im}(g))^2$, showing a sinc-squared frequency dependence through $g(\Delta\beta)$, which does not allow for efficient and broadband FWM. Ideally, g is real-valued over the pump bandwidth, and satisfies the condition $\delta\beta_p \le 4\gamma P_p$, with the central pump frequency set to obtain a dispersion induced phase mismatch which cancels the nonlinear contribution, i.e. $\Delta\beta = -2\gamma P_p$. For λ_s = 1547 nm, S_1 fulfills the real-value condition for g, for pump bandwidth $\Delta\lambda_p$ < 15 nm, whereas for S_2 the result is $\Delta\lambda_p$ < 1.5 nm. Hence, for broadband chirped-pump FWM, the dispersion slope becomes an important optimization parameter.

Optics EXPRESS

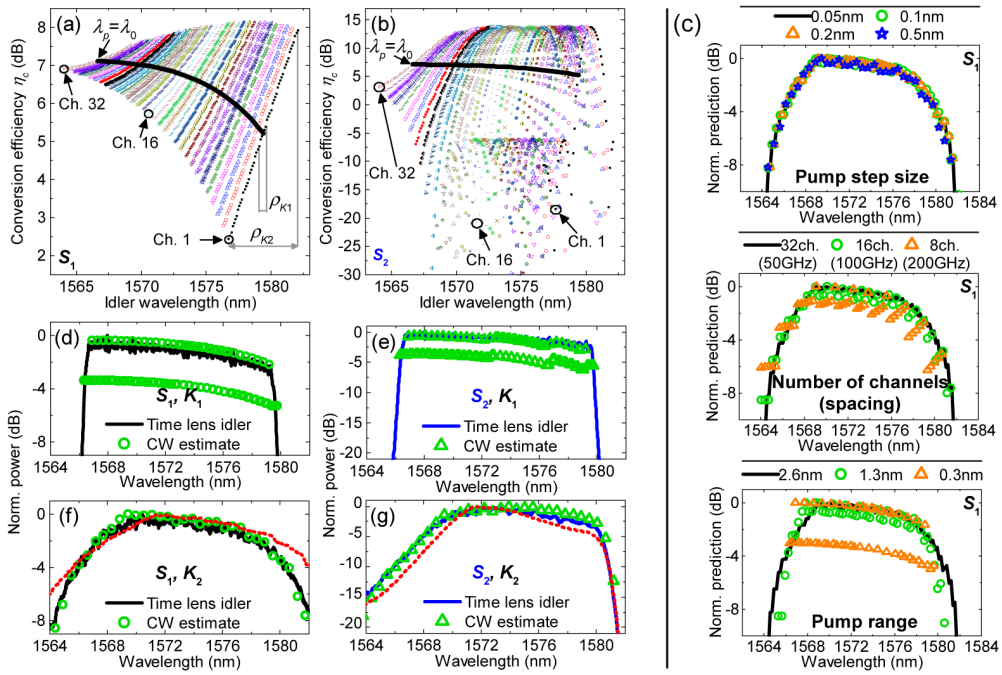

Fig. 3. (a), (b) CW conversion efficiency simulations for dispersion slopes S_1 and S_2, grouped by channel position. Black line indicates simulations at $\lambda_p = \lambda_0$. (c) CW estimates for varied simulation parameters. (d)-(g) Simulated time lens spectra (solid lines) for different pump chirp and dispersion slope combinations, and CW estimates using the CW efficiency data (symbols). In (f), (g) the red dotted line is estimate for full pump bandwidth $\Delta\omega_p$.

To estimate the chirped-pump FWM bandwidth and per-channel efficiency for both HNLFs, a series of CW FWM simulations are performed via the SSFM. The generated idler power is calculated for the CW signal placed at each of the WDM channel positions in sequence, and for the CW pump swept over a range of 4.8 nm in steps of 0.05 nm, centered at 1560 nm. Thus, the aggregate simulated data includes contributions at wavelengths covering the entire flat-top part of the pump spectrum, for both pump cases. The CW pump power is set to match the peak chirped pulsed power of 26.3 dBm, and the signal power is set to −15 dBm. The simulated input conversion efficiencies, η_c, as a function of the idler wavelength, are shown for S_1 in Fig. 3(a). A symbol shape denotes a WDM channel position, and the thick black line marks data points where $\lambda_p = \lambda_0$, and the efficiency is the same for S_1 and S_2. The data points generated for the parts of the pump spectrum which do not overlap temporally with the signal, are excluded. As a convenient approximation, only the FWHM of the signal duration is considered, and the pump wavelength dependent efficiencies are weighted equally (implying constant signal power), even though the signal power has a Gaussian distribution. The extent of pump wavelengths overlapping temporally with the signal is estimated to be $\Delta\lambda_{p,1} \times \Delta t_s/\Delta t_p \approx 0.3$ nm for Pump$_1$ and $\Delta\lambda_{p,2} \times \Delta t_s/\Delta t_p \approx 2.6$ nm for Pump$_2$. The subsets of channel 1 data points used for the characterization at different pump chirp rates, are indicated for Pump$_1$ (ρ_{K1}) and Pump$_2$ (ρ_{K2}). Compared to the conversion efficiencies shown for S_2 in Fig. 3(b), the η_c values for the small slope, S_1, are relatively uniform around λ_0. To predict the chirped pump FWM idler shape, the CW efficiency data for each converted channel is linearly interpolated onto a common 100-point grid of wavelengths from the lowest to the highest idler wavelength of the data set (extrapolated values are null). Then, the interpolated values are combined by element-wise addition, to estimate the combined idler shape for all converted WDM channels. The resulting normalized estimates for S_1 are shown in Fig. 3(c), with varied pump step size, number of signal wavelengths and range of pump wavelengths.

Optics EXPRESS

The parameters are varied one at a time, with basis parameters of 0.05 nm step size, 32 channel positions and 2.6 nm pump wavelength range. Changing the pump step size from 0.05 nm to 0.5 nm does not significantly change the result, since the linear interpolation in this case can predict the efficiency with high accuracy (see Fig. 3(a)). Hence, in this case the pump step granularity can be increased significantly with low loss of accuracy. As the number of channel positions are reduced from 32 to every fourth channel (8 channels), the overall shape remains approximately the same. The estimated shape becomes less smooth because the channel spacing increases, thus decreasing overlap between nonnull data points for different channels. Hence, the transitions become more abrupt when the sum is calculated. Varying the pump range from 2.6 nm ($Pump_2$) to 0.3 nm ($Pump_1$) results in reduced idler bandwidth, which is expected because a lower pump chirp rate is implied. However, as the pump range is reduced, the nonnull data point overlap for different channels is again reduced. At 0.3 nm pump range, the data points originate from values of λ_p close to the ZDW, and only points for neighboring channels overlap. The overlapping data points at the converted-channel wavelength boundaries have approximately equal efficiency, resulting in zigzag-like ~3-dB transitional artifacts. In effect, two similar curves are created with a vertical ~3-dB shift. To compare with the time lens simulation results, the normalized CW estimates (symbols) are superimposed on top of the chirped pump FWM idler spectrum for $Pump_1$, in Figs. 3(d) and 3(e). Here the (upper) artifact curves are easily identified by visual inspection. The corresponding CW estimates for $Pump_2$ are shown in Figs. 3(f) and 3(g), which closely resemble the time lens idler shapes. The dotted lines show estimates which include data for the entire 1-dB pump bandwidth (4.8 nm instead of 2.6 nm), yielding less accurate results as expected.

To make a simple estimation of the absolute per-channel WDM-OTDM conversion efficiencies, the CW efficiency data is averaged for each CW signal position. For comparison, the conversion efficiency for each WDM channel is calculated by simulating chirped pump FWM for a single-channel input. The results for slope S_1 (circles) in Fig. 4(a), show differences <0.18 dB for $Pump_1$ and <0.13 dB for $Pump_2$ for all channels, indicating good agreement between the CW estimates and the chirped pump FWM efficiencies.

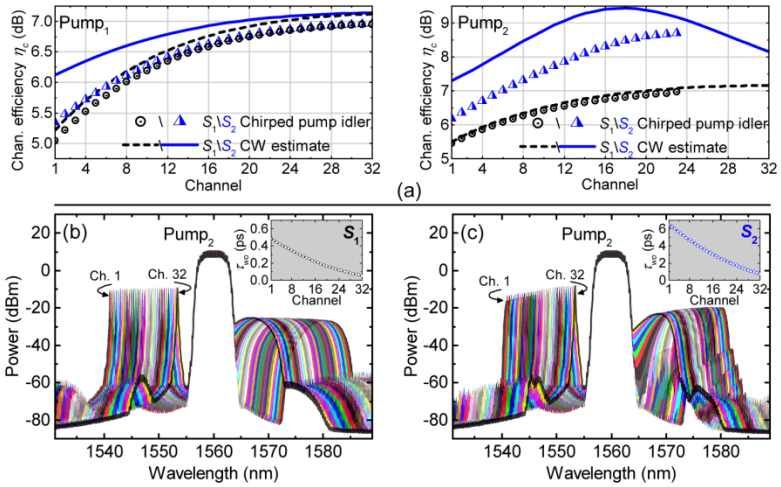

Fig. 4. (a) Chirped pump FWM channel conversion efficiency (lines) and corresponding predictions using the CW characterization estimates (symbols) for different dispersion slopes and pump chirp rates. (b)-(c) Spectra for chirped pump FWM conversion of individual channels for different dispersion slopes with pump chirp rate $K_2/2$. Insets show the channel walkoff.

However, the results for slope S_2 (triangles) are less accurate, showing differences of up to 0.7 dB and 1.2 dB for $Pump_1$ and $Pump_2$ respectively. Note that, due to the risk of pump

Optics EXPRESS

spectral leakage affecting the calculation, the time lens efficiencies for converted WDM channels overlapping spectrally with $Pump_2$ (Ch. 24-32) are omitted. The simulated chirped pump FWM spectra for the individually converted WDM signals are visualized for S_1 in Fig. 4(b) and for S_2 in Fig. 4(c). The insets show the walkoff of the WDM channels relative to the pump pulses, τ_{wo}, as a function of the channel position. Here, the walkoff is derived from the Taylor expansion of the group delay, β_1, and can be written as,

$$\tau_{wo} = \left[\beta_2 \left(\omega_s - \omega_p \right) + \frac{\beta_3}{2} \left(\omega_s - \omega_p \right)^2 + \frac{\beta_4}{6} \left(\omega_s - \omega_p \right)^3 \right] L. \qquad (3)$$

The single-channel chirped-pump FWM idler spectra are highly uniform for S_1, whereas distortions due to the dispersion slope are clearly visible for S_2. The reduced per-channel efficiency estimate accuracy for slope S_2 is expected to be related to the pump-signal walkoff. The channel 1 walkoff for S_1 is negligible at 0.5 ps. However, due to the TOD dependence, the walkoff is 6.5 ps for S_2, which is equivalent to a ~0.4-nm shift of the local pump wavelength for $Pump_2$. Small pump wavelength changes to the local signal-overlap during propagation may have a significant impact on the phase mismatch, and the effect is not predicted by the CW characterization method. However, the simulation results indicate that the CW characterization method can provide reasonably accurate estimates for both the chirped pump FWM idler shape and per-channel efficiencies in HNLF; even for relatively large dispersion slopes. Additionally, very accurate predictions are indicated for fibers with low dispersion slope, which are better suited for chirped pump FWM. Using this method, HNLFs can be characterized for many time lens scenarios, or optimized for one; e.g. by sweeping the CW pump and signal over a large wavelength range, and selecting appropriate data subsets to make estimates for different scenarios. Finally, the method can potentially be adapted to characterize HNLF for other time lens schemes based on chirped pump FWM. For example, OTDM-to-WDM conversion [6], is based on the same physical mechanisms, although in this case each pump pulse overlaps with multiple OTDM pulse tributaries, which are also chirped from dispersion D. Hence, it becomes more challenging to track which pump and signal frequencies interact, and depending on the signal chirp and pulse shape, it may no longer be a valid approximation to assume that the power of tributary frequencies interacting with different pump frequencies is the same. Nevertheless, the procedure to characterize a fiber for WDM-OTDM yields the necessary data to characterize it for OTDM-to-WDM conversion as well. Compared to the characterization of a fiber for WDM-OTDM conversion, a decreased pump step size may be necessary for a detailed OTDM-to-WDM characterization, because the low duty cycle OTDM tributaries each mix with a smaller fraction of the pump spectrum. Conversely, as the OTDM signal is centered around a single wavelength, it may be sufficient to measure the efficiency at only one or a few frequencies over the signal bandwidth. Hence, the total number of CW characterization measurements does not necessarily increase, although complexity is added to the subsequent data processing. Further analysis is necessary to determine the specific requirements for CW characterization of different scenarios, although that is beyond the scope of this paper.

Optics EXPRESS

3. Composite DF-HNLF optimized for efficient broadband chirped pump FWM

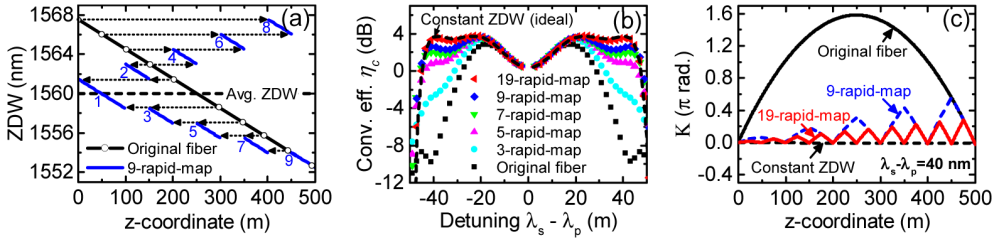

Fig. 5. (a) Illustration of rapid-map segmentation into 9 pieces and rearrangement of original fiber with a linear ZDW variation. (b) Conversion efficiency simulations for original fiber and various rapid-map configurations. (c) Illustration of the rapid-map effect on the cumulative phase mismatch at 40 nm detuning.

As we have shown, a fiber optimized for a broadband, FWM-based time lens has a low dispersion slope. Thus, similar phase mismatch for frequencies within the pump bandwidth can be achieved. DF-HNLF have a nonlinear coefficient close to standard HNLF, and are designed for very low slopes [16]. However, core geometry variations from e.g. the preform drawing process, can cause the ZDW to fluctuate considerably in the longitudinal direction of the fiber. Hence, the FWM bandwidth and efficiency may be significantly reduced [18]. Indeed, the ZDW may vary on the order of tens of nanometers over a few hundred meters in DF-HNLF [17]. To manage the dispersion fluctuations, we propose to rearrange fiber segments with different local dispersion into a "rapid-map" configuration [21], as illustrated in Fig. 5(a). Here the ZDW of the original fiber varies by 15 nm over 500 m, with average λ_0 = 1560 nm. For simplicity, the chosen variation is linear in the longitudinal z-direction. The shown 9-rapid-map is segmented into 9 pieces, arranged so that the combined dispersion of adjacent segment pairs, matches the average dispersion over the entire fiber length. Thus, the local ZDW oscillates, causing the dispersion to periodically reverse sign at the mean ZDW. To investigate the rapid-map effect, the FWM conversion efficiency, η_c, is simulated as a function of the pump-signal detuning for a 500-m DF-HNLF with 15-nm linear ZDW variation, as in Fig. 5(a). The dispersion slope and nonlinear coefficient have typical values of S = 0.005 ps/(nm^2·km), and γ = 10.8 (W·km)$^{-1}$ respectively. The pump and signal are 50% duty cycle (DC) return-to-zero pulses with 10 GHz repetition rate and negligible walkoff. The pump peak power is P_p = 25 dBm and the wavelength is 1565 nm; the signal power is in the small-signal regime. The ZDW variations are modelled as vertical translations of the group velocity dispersion, β_2, vs. frequency curve [29], and higher order dispersion coefficients are assumed constant. The conversion efficiency results are shown for the original fiber, and for different rapid-map configurations in Fig. 5(b). For reference, the ideal results without dispersion fluctuations are shown as well (dashed). The bandwidth is improved for all rapid-maps, with greater benefit for a larger number of (shorter) segments. For a 19-rapid-map consisting of 25-m segments, almost ideal bandwidth is obtained. The rapid-map effect can be explained by considering the cumulative phase mismatch, K(z), including the nonlinear phase contribution and up to fourth order dispersion defined as,

$$\mathrm{K}(z) \equiv 2\gamma P_p z + \int_0^z \Delta\beta(z')dz'. \tag{4}$$

Here fiber loss and pump depletion is assumed to be negligible. Equation (4) is plotted in Fig. 5(c) at 40 nm detuning, for the original fiber, with and without fluctuations, and for the 9- and 19-rapid-maps. Without fluctuations K(z) ≈0 rad., indicating optimum FWM efficiency, whereas the original fiber generally exhibits poor phase matching conditions. For the rapid-map assemblies with alternating dispersion sign, the phase mismatch periodically returns to

Optics EXPRESS

the average (ideal) dispersion case, thus avoiding the accumulation of a large phase mismatch. Naturally, the period decreases for an increasing number of segment pairs, which reduces the mean value of K(z) and improves the overall efficiency. As a practical consideration, it is important to investigate the impact of splice losses for segmented HNLF. Therefore, the simulation model was adapted to include splice losses at the interface between HNLF segments. The simulated efficiency curves for the 19-rapid-map with losses per splice from 0 to 0.5 dB, are shown in Fig. 6(a). The results indicate that splice losses close to 0.01 dB should be achieved to avoid significant efficiency reductions with 19 segments. Figure 6(b) shows the efficiency, with the pump power increased to maintain an average of 25 dBm peak pump power in the fiber. Assuming extra pump power is available, the efficiency loss can be compensated relatively well for low splice losses. However, the bandwidth is significantly reduced at 0.5 dB loss per splice, indicating that there is a tradeoff between efficiency loss compensation and bandwidth. This could limit the applicability of fiber segmentation to fiber types with similar mode profiles. The loss of maximum efficiency as a function of the per-splice loss, normalized with respect to the total splice losses, is shown in Fig. 6(c) for 5-, 13- and 19-rapid-maps. The normalized efficiency losses are similar with per-splice losses <0.1 dB for the different rapid-maps, indicating that the efficiency loss scales approximately linearly with the splice losses. However, the behaviors diverge towards larger splice losses, where the accumulated nonlinear effects due to the losses play an increasing role.

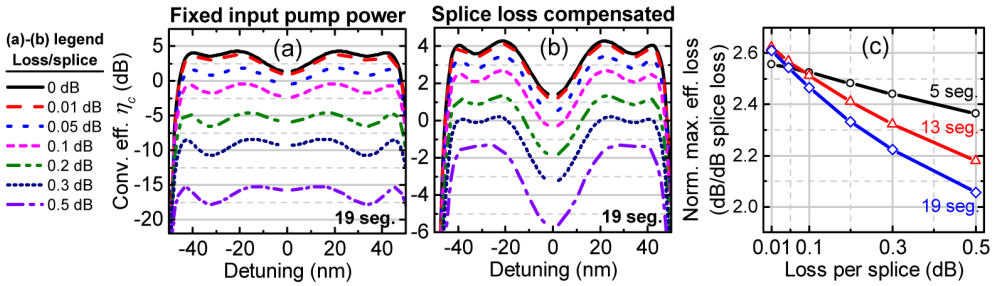

Fig. 6. (a) Conversion efficiency vs. pump-signal detuning for the 19-rapid-map with different HNLF-to-HNLF splice losses and fixed P_p = 25 dBm. (b) The conversion efficiencies for the pump power increasing with the splice losses. (c) Max. efficiency loss normalized by the total splice losses vs. the loss per splice (fixed P_p).

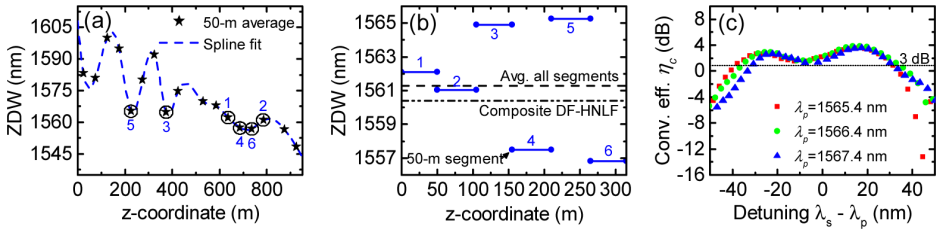

Fig. 7. (a) ZDW measurements for 50-m DF-HNLF segments. Numbered data points indicate order of assembly for rapid-map. (b) ZDW map for composite DF-HNLF in rapid-map configuration. (c) CW input conversion efficiency measurements for composite DF-HNLF with 28 dBm pump power at different pump wavelengths.

To create a composite DF-HNLF in a rapid-map configuration optimized for broadband time lens applications, a 1-km DF-HNLF piece with suitable average ZDW was selected, and divided into 50-m segments. To obtain the dispersion parameters, the group delay was measured for each segment using an Agilent 86037C dispersion test set. The dispersion at 1550 nm was very small (<0.005 ps/nm), and hence repeated measurements were averaged to lower the uncertainty. Finally, the dispersion parameters were derived from a five-term

Optics EXPRESS

Sellmeier polynomial fitted to the group delay [30]. The ZDW distribution is shown in Fig. 7(a), and as expected, the ZDW variation over 1 km is large (~50 nm). Six segments were chosen to assemble a composite fiber in a rapid-map configuration. The average HNLF-to-HNLF splice loss was only around 0.03 dB using a standard fusion splicer program, and the combined splice losses due to SSMF pigtails was 0.7 dB (0.35 dB per fiber end with bridge fibers). Including propagation losses, the total insertion loss was ~1 dB. The composite DF-HNLF rapid-map is shown in Fig. 7(b), with the segments chosen to obtain an average ZDW close to 1561 nm for FWM conversion between the C- and L-bands. The measured composite fiber parameters were $L = 315$ m, $\gamma = 10.8$ (W·km)$^{-1}$, $\lambda_0 = 1560.4$ nm, $S = 0.0045$ ps/(nm^2·km) and $\beta_4 = 2.4 \times 10^{-4}$ ps^4/km. Over 8 group delay measurements, the standard errors for the derived dispersion values were $\sigma_{\lambda 0} = 0.1$ nm, $\sigma_S = 4 \times 10^{-5}$ ps/(nm^2·km) and $\sigma_{\beta 4} = 5 \times 10^{-6}$ ps^4/km, for the ZDW, the slope and the fourth order dispersion respectively. Note that the average segment ZDW is slightly higher than the measured composite DF-HNLF ZDW; to accurately predict the ZDW for a composite fiber, the zero-crossing as determined from the mean dispersion curve is required. Finally, CW input conversion efficiency spectra were measured as a preliminary characterization, using a standard setup (see Fig. 8(a) in the next section on CW characterization). The small-signal results with 28 dBm pump power are shown in Fig. 7(c), for pump wavelengths varied over 2 nm, indicating uniform performance and ~70 nm 3-dB bandwidth with >0 dB efficiency.

4. Experimental characterization of HNLF for WDM-OTDM conversion

In the following, we consider two different HNLFs used for two WDM-OTDM conversion scenarios. The HNLFs are characterized using the CW method, and the results are compared to the corresponding time lens results. The first scenario is the present demonstration of the composite DF-HNLF (HNLF1), for WDM-OTDM conversion of 32 WDM channels using a broadband chirped pump [24]. The second scenario is for a standard HNLF (HNLF2), previously used for 8- and 16-channel WDM-OTDM conversion [25].

CW characterization of nonlinear fibers for WDM-OTDM conversion scenarios

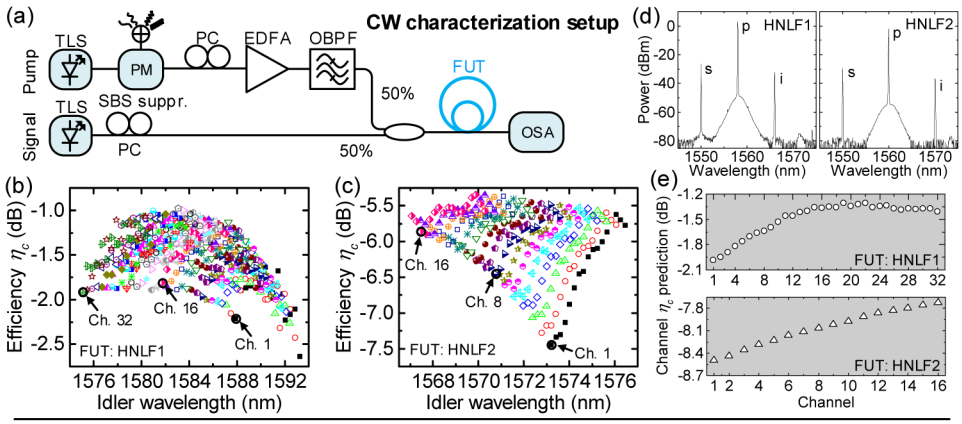

HNLF1 is a composite DF-HNLF characterized for time lens conversion of 32 10-Gbaud WDM channels with 50 GHz spacing.
HNLF2 is a standard HNLF characterized for time lens conversion of 8/16 10-Gbaud WDM channels with 100 GHz/50 GHz spacing.

Fig. 8. (a) Setup for CW characterization of HNLF for chirped pump FWM. (b) Sample FWM spectra for HNLF1 and HNLF2. (c) CW measurements for bandwidth estimation of 32-channel conversion using 2.6 nm chirped pump in HNLF1. (d) CW measurements for estimation of 8- and 16-channel conversion using a 1.6 nm chirped pump in HNLF2. (e) Channel conversion efficiency predictions for HNLF1 and HNLF2.

The HNLF characterization setup for time-lens-scenario performance estimation, is based on a standard CW FWM measurement setup, as shown in Fig. 8(a). The pump is generated from

Optics EXPRESS

a CW tunable laser source (TLS), which is phase modulated using 4 radio frequency tones for efficient SBS suppression [31]. Then, the CW pump is amplified to match the peak chirped pulse pump power at the input to the fiber-under-test (FUT), corresponding to the chirped pump FWM experiment that the FUT is characterized for. ASE noise is removed using a narrow filter to avoid interference with the signal or idler, and the pump is coupled into the FUT using a 3-dB coupler. The signal is generated from a TLS, which couples −6 dBm power into the FUT after the 3-dB coupler. The signal power roughly corresponds to the WDM per-channel power. Finally, the FWM spectrum is measured at the FUT output. The pump wavelength is tuned over the bandwidth, which is estimated to overlap with the signal of the corresponding time lens experiment, and the signal placed sequentially at the WDM channel positions.

The first characterization is for the composite DF-HNLF (HNLF1), which was introduced in the previous section. In this case, the fiber is used for a chirped-pump FWM experiment, with a WDM signal consisting of 32 channels, centered from 1540.16 nm to 1552.52 nm on a 50 GHz grid. The chirped pump for the time lens experiment has ~26.3 dBm peak power, and an estimated flat-top bandwidth of 4.8 nm centered at 1565 nm, of which 2.6 nm are estimated to overlap temporally with the signal. The CW characterization results are shown in Fig. 8(b), for the CW pump swept over 2.6 nm around 1565 nm in 0.2 nm increments, with the CW signal placed at each of the WDM channels positions. The conversion efficiency varies by <1 dB per channel over the range of pump wavelength contributions, indicating that the channels can be converted via chirped-pump FWM without significant distortions. Importantly, the efficiencies do not change significantly vs. channel, indicating that the channels are all within the attainable time lens bandwidth of HNLF1.

The second characterization is for an OFS standard HNLF (HNLF2) with parameters L = 500 m, γ = 11.3 $(\mathrm{W{\cdot}km})^{-1}$, λ_0 = 1561 nm, and S = 0.017 $\mathrm{ps/(nm^2{\cdot}km)}$. HNLF2 was used for WDM-OTDM conversion of 16 and 8 (odd channels) WDM channels on 50- and 100-GHz grids respectively, from 1547.40 nm to 1553.32 nm. The chirped pump had 20.1 dBm peak power with 1.6-nm flat-top bandwidth centered at 1561 nm, which fully overlapped with the signal. The CW pump was swept in 0.1 nm increments around 1561 nm, with the CW signal placed at each of the 16 WDM channel positions. The CW characterization results for HNLF2 are shown in Fig. 8(c), indicating per-channel efficiency differences depending on the pump wavelength of 0.5 dB (Ch. 16) to 2.0 dB (Ch. 1). Hence, a reasonably uniform performance is expected for all channels, which should fit within the attainable time lens bandwidth of HNLF2.

Representative measured CW FWM spectra for the fibers are shown in Fig. 8(d). In Fig. 8(e) the estimated per-channel conversion efficiencies are shown for both time lens experiments, calculated as the average pump wavelength dependent efficiency. The maximum channel conversion efficiency differences are estimated to be <0.7 dB for all 32 channels in HNLF1 and <0.8 dB for all 16 channels in HNLF2. Note that for HNLF2, the averaged channel efficiency predictions are reduced by 2.1 dB, corresponding to the ratio of the pump- and signal duty cycles. This duty cycle mismatch causes a pulse carving of the signal, which reduces the average power of the converted signal. In the following subsections, the WDM-OTDM scenarios are described in greater detail, and compared to the corresponding CW estimates.

Optics EXPRESS

WDM-OTDM conversion scenario using a composite DF-HNLF

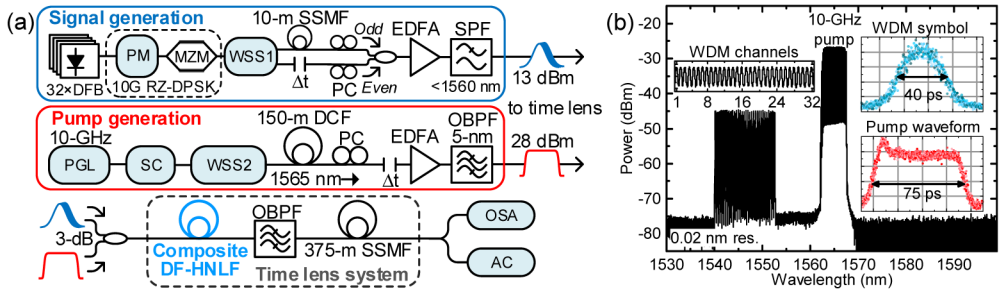

Fig. 9. (a) Setup for conversion of 32 WDM channels in time lens based on FWM in the composite DF-HNLF. (b) Spectrum at input to the composite DF-HNLF with insets showing the measured WDM and pump waveforms.

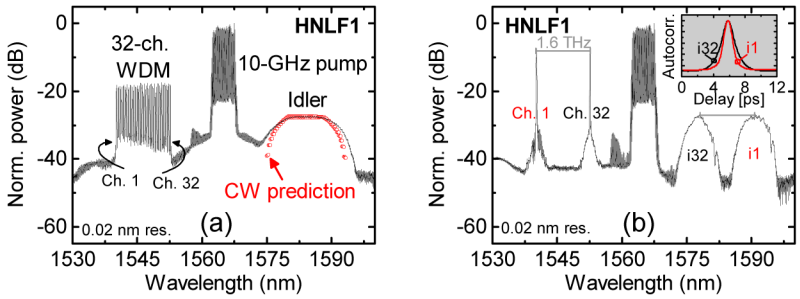

Fig. 10. (a) Chirped-pump FWM spectrum with 32-channel WDM input in HNLF1, and the estimated idler shape as predicted from CW characterization. (b) Chirped-pump FWM spectrum for channels 1 and 32 only. Inset shows the converted channel autocorrelations after 375 m SSMF.

To demonstrate the potential of the composite DF-HNLF, HNLF1, it is used in an experiment for the conversion of 32 WDM channels using a broadband chirped FWM pump. The setup is shown in Fig. 9(a). Here a WDM signal is generated from an array of 32 distributed feedback (DFB) lasers with 50 GHz spacing, centered from 1540.16 nm to 1552.52 nm. The CW lines are DPSK modulated at 10 Gbit/s with a $2^{31} - 1$ pseudo-random bit sequence (PRBS) in a phase modulator (PM), and pulse carved to generate return-to-zero (RZ) pulses with ~50% duty cycle in a Mach-Zehnder modulator (MZM). The even and odd channels are separated using a wavelength selective switch (WSS1) with 14-GHz, 3-dB Gaussian channel filters, and decorrelated by delaying the odd channels ~500 symbols, before recombination with the even channels. After WSS1, the WDM pulse width is ~40 ps. Then, the WDM signal is amplified to 13 dBm average power in an erbium-doped fiber amplifier (EDFA). Finally, amplified spontaneous emission (ASE) noise above 1560 nm is suppressed using a Koshin Kogaku shortpass filter (SPF), to avoid interference at the idler wavelength. The pump source is an erbium-glass oscillating, pulse generating laser (PGL) at 1542 nm, generating 10-GHz pulses with ~1.5 ps FWHM. The pulses are amplified to 23 dBm average power, and propagated in 400 m DF-HNLF (1542 nm << λ_0), to generate a self-phase modulation induced supercontinuum (SC), from which a 600 GHz (4.8 nm) 3-dB bandwidth, 10th order super-Gaussian spectrum is carved out using WSS2. Then, the pump pulses are broadened to 75 ps FWHM by propagation in 150 m dispersion-compensating fiber (DCF), thus obtaining a chirp rate of 0.05 ps^{-2}. Then, the pump is amplified to 28 dBm average power, with subsequent pump ASE noise suppression in a flat-top 5-nm optical bandpass filter (OBPF). To generate a signal copy at the idler wavelength with chirp rate $K = 0.1$ ps^{-2} by FWM, the signal and pump are combined in a 3-dB coupler, and launched into the composite DF-HNLF. The input

Optics EXPRESS

spectrum is shown in Fig. 9(b), with insets showing oscilloscope traces of the WDM symbol and pump waveforms, and a zoom-in of the WDM channels. The generated idler is separated from the signal and pump using a broad, flat-top OBPF, and propagated in 375 m standard single-mode fiber (SSMF), with accumulated dispersion $D = -1/K$. Thus, the idler pulses are simultaneously compressed and aligned, to fit within ~3.1 ps time slots at the output. Note that the dispersion and chirp rate have opposite signs, due to phase conjugation of the signal. Finally, the spectrum is measured using an optical spectrum analyzer (OSA), and the pulses are characterized using an autocorrelator (AC). The FWM spectrum at the output of the composite DF-HNLF is shown in Fig. 10(a), with the normalized (with respect to the maximum idler power) estimate based on CW efficiency measurements for HNLF1 superimposed for comparison. The idler spectrum is widely flat-topped with a high degree of symmetry, indicating uniform conversion, with a measured –4.6 dB WDM input conversion efficiency. The predicted shape and idler spectrum are in good agreement, with a 16% 3-dB bandwidth difference. The FWM spectrum for channels 1 and 32 enabled is shown in Fig. 10(b). The inset shows idler AC traces after 375 m SSMF, indicating 1-1.2 ps pulse FWHM. The converted channels are very similar, with a 0.8 dB efficiency difference. The efficiency difference is close to the predicted value of 0.7 dB (cf. Figure 8(e)), although the absolute efficiency values are 2.3 dB lower than predicted.

WDM-OTDM conversion scenario using a standard HNLF

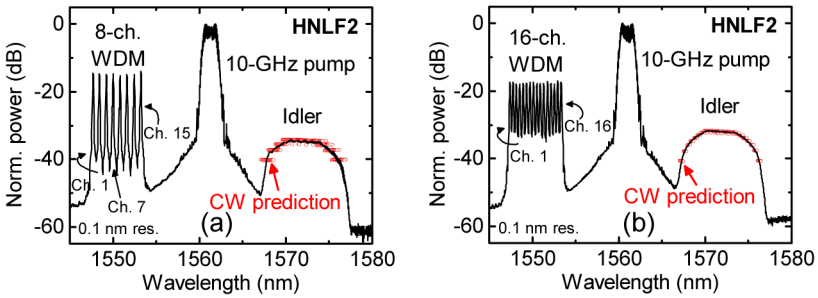

Fig. 11. (a)-(b) FWM spectra at the output of HNLF2 for 8 and 16 channels, and their respective idler shape predictions.

HNLF2 was used for WDM-OTDM conversion of 8 and 16 10-Gbaud DPSK modulated WDM channels, without additional pulse carving (hence the WDM symbols are flat-top with high duty cycle) [25]. The channel spacings are 50 GHz and 100 GHz for 16 and 8 channels respectively, centered from 1547.40 nm to 1553.32 nm. The pump consisted of chirped rectangular-like pulses at 10 GHz repetition rate, with 1.6 nm 1-dB bandwidth at 1561 nm, 55 ps FWHM and 20.1 dBm peak power. The 8-channel FWM spectrum is compared to the corresponding CW estimate in Fig. 11(a). Although the prediction forms a step-like function due to the relatively low channel overlap after conversion, the symmetry around the idler spectrum enables accurate inference of the idler shape and bandwidth. The predicted 16-channel FWM spectrum with 50 GHz channel spacing shown in Fig. 11(b), is in excellent agreement with the corresponding time lens experiment as well. Hence, the comparisons for both HNLF1 and HNLF2, show that the WDM-OTDM conversion bandwidth can be accurately estimated, based on simple CW characterizations.

5. Conclusion

Using detailed numerical simulations and experimental demonstrations, we have investigated and verified a novel method for the characterization of HNLF for chirped pump FWM, based on mixing of only two tunable CW lasers. The method enables accurate determination of the time lens bandwidth for WDM-OTDM conversion based on OFT, by discretizing the chirped

Optics EXPRESS

pump FWM process into a set of constituent processes, and can potentially be adapted for other OFT scenarios such as OTDM-WDM conversion. The investigation showed that the dispersion slope is a critical fiber parameter for the optimization of HNLF for time lens applications requiring a broadband pump. Hence, a composite dispersion-flattened HNLF was assembled, with a dispersion rapid-map optimized to mitigate FWM impairments due to longitudinal dispersion fluctuations of the fiber. The fiber was used for the uniform and efficient conversion of 32 WDM channels with 50 GHz spacing using a broadband chirped pump, achieving −4.6 dB input efficiency with an observed 0.8 dB channel efficiency variation. The demonstrated methods are intuitive and simple to use, and show promise as tools for the optimization of broadband chirped pump FWM in HNLF.

Funding

Danish Council for Independent Research (DFF) NANO-SPECs project (DFF-4005-00558B).

Acknowledgments

The authors gratefully acknowledge OFS for providing nonlinear fibers and facility access.